



## Effects of rib spacing and height on particle deposition in ribbed duct air flows

Hao Lu, Lin Lu\*

Department of Building Services Engineering, The Hong Kong Polytechnic University, Hung Hom, Kowloon, Hong Kong, China



### ARTICLE INFO

#### Article history:

Received 24 March 2015

Received in revised form

28 April 2015

Accepted 29 April 2015

Available online 14 May 2015

#### Keywords:

Particle deposition

Surface ribs

Deposition enhancement

RSM model

CFD

### ABSTRACT

In this study, the influences of rib spacing and height on particle deposition in ribbed duct air flows were numerically investigated. The turbulent air flow was resolved using the Reynolds stresses model (RSM) with turbulent fluctuation correction, while the particle phase was tracked by the discrete particle model (DPM). The ratios of rib spacing to rib height  $p/e$  were 2, 4, 6, 8 and 10 while the ratios of rib height to duct diameter  $e/D$  were 0.05, 0.1 and 0.2. The air flow velocity profiles for both smooth and ribbed ducts as well as particle deposition velocity in a smooth duct obtained in the simulation agree well with previous related study data. It is found that particle deposition velocity is significantly enhanced by the surface ribs for several orders of magnitude, especially for small particles ( $\tau_p^+ < 1$ ). Particle deposition enhancement increases with the decreasing rib spacing, while no significant difference is found for different rib heights. The mechanisms of particle deposition enhancement were analyzed and discussed in relation to different rib spacings and heights. Moreover, an efficiency ratio has been defined to evaluate the particle deposition enhancement ratio together with the increase of flow drag. The maximum efficiency ratio can reach about 1000 for small particles ( $\tau_p^+ < 1$ ) and about 100 for large particles ( $\tau_p^+ > 1$ ) when  $p/e = 2$  and  $e/D = 0.1$ . Therefore, a reasonable arrangement of surface ribs is an efficient and effective choice for enhancing particle deposition, and could be adopted in air filtration devices.

© 2015 Elsevier Ltd. All rights reserved.

### 1. Introduction

Suspended aerosol particles have become a serious health threat particularly in industrialized regions. Such particles are obviously present in varying degrees both indoors and outdoors. The maintenance of indoor air quality (IAQ) is important as people generally spend more time indoors and usually in a comparatively confined space. Therefore, better understanding of aerosol particle flows and efficient particle filtration devices are crucial for the maintenance and further improvement of IAQ. Surface ribs, popularly applied for heat transfer enhancement, have also been found to be effective and efficient in the enhancement of particle collection performance in air electrostatic precipitators (ESP) [1,2]. The arrangement of the repeated surface ribs in ventilation ducts offers a potential filtration method to improve air quality by intercepting aerosol particles [3,4]. In a previous study conducted by the authors [5], it was found

that particle deposition could be significantly enhanced by rib interception and the entrainment of turbulent eddies. However, the pressure drop of the air flow is also increased for the extra form drag of the surface ribs. Rib spacing and height were found to be two crucial parameters in the determination of the particle deposition enhancement performance and also flow drag increase. Therefore, the influences of rib geometry parameters on the comprehensive performance of particle deposition enhancement need to be evaluated by studying the above effects together. Such research is valuable and meaningful to IAQ improvement and other related engineering applications.

A few studies have been conducted on particle deposition enhancement engendered by surface ribs. Lai et al. [3,4] investigated the particle deposition rate in ribbed duct air flows by means of experiments. The results showed that particle deposition was significantly enhanced by the surface ribs. The rib pitch-to-height ratio was 10 and the rib height-to-duct diameter ratio was 0.04 in the experiments. Recently, Barth et al. experimentally investigated multilayer particle deposition in a ribbed duct flow [6]. The particle deposition enhancement, however, was not investigated. Several

\* Corresponding author. Tel.: +852 34003596.

E-mail address: [vivien.lu@polyu.edu.hk](mailto:vivien.lu@polyu.edu.hk) (L. Lu).

numerical studies have been conducted on particle deposition and transport in obstructed flows or ribbed surface flows [7–10]. From these studies, it was found that a large number of particles were intercepted on the windward side of the obstructions or surface ribs, while the rib geometry parameters remained unaltered. It has been confirmed that particle deposition rate could be enhanced by surface ribs. However, it should be noted that all rib geometry parameters were constant in previous studies. The focus of this study is the investigation of the effects of both rib spacing and rib height on particle deposition enhancement performance and also the pressure drop increase of the air flow.

Chen [11] noted that in recent years, numerical simulation, based on the computational fluid dynamics (CFD) approach had become a powerful tool in the investigation of building environment problems such as particle deposition and IAQ. In general, the accurate measurement of particle behavior and deposition in complex turbulent air flows are quite challenging for experiments, while it could be numerically predicted with suitable CFD models [12,13]. For aerosol particle flows, the Eulerian-Lagrangian methods have been proved as effective and credible models to predict particle deposition in turbulent flow by many researches [14–18]. In the above frames, accurate prediction of turbulent air flow is crucial to successfully obtain the particle deposition velocity [15,16]. Compared with Reynolds-averaged Navier–Stokes (RANS) models, direct numerical simulation (DNS) or large eddy simulation (LES) have been still unsuitable for engineering application due to their high computational cost. In addition, it was found that the RANS model with velocity fluctuation correction can already accurately predict the deposition velocity of particles with 0.1–50 μm in turbulent flow [19–22]. Tian and Ahmadi [16] compared the simulation results of particle deposition in turbulent duct flow for different turbulence models. They found that the Reynolds stress model (RSM) with velocity fluctuation correction can obtain a more accurate particle deposition velocity than other RANS models. A possible reason is that RSM takes turbulence anisotropy into account while most eddy viscosity models simply assume isotropic turbulence structures. RSM with turbulent fluctuation correction, therefore, is adopted in this study. The objective is to establish the surface rib spacing and height for high particle deposition enhancement with low pressure drop increase. Moreover, the mechanisms of particle deposition enhancement due to the surface ribs were also studied and further discussed in relation to the interceptions of ribs, deposition areas and turbulent structures.

## 2. Numerical model and methodology

### 2.1. Turbulent air flow and particle motion models

In this study, turbulent air flow fields were solved using the RSM model with velocity fluctuation correction. The particle phase was governed by the discrete particle model (DPM). For turbulent duct flow, the mean mass and momentum equations for turbulent air flow can be expressed as,

$$\frac{\partial \bar{u}_i}{\partial x_i} = 0, \quad (1)$$

$$\frac{\partial \bar{u}_i}{\partial t} + \bar{u}_j \frac{\partial \bar{u}_i}{\partial x_j} = -\frac{1}{\rho} \frac{\partial \bar{p}}{\partial x_i} + \frac{1}{\rho} \frac{\partial}{\partial x_j} \left( \mu \frac{\partial \bar{u}_i}{\partial x_j} - \rho \bar{u}'_i \bar{u}'_j \right), \quad (2)$$

where  $\bar{u}_i$  and  $\bar{p}$  are the time-averaged velocities and pressures, respectively.  $\mu$  is the air dynamic viscosity. The equation of the Reynolds stress  $\rho \bar{u}'_i \bar{u}'_j$  is described by,

$$\begin{aligned} \frac{\partial}{\partial t} \left( \bar{u}'_i \bar{u}'_j \right) + \bar{u}_k \frac{\partial}{\partial x_k} \left( \bar{u}'_i \bar{u}'_j \right) &= \underbrace{\frac{\partial}{\partial x_k} \left( \frac{\nu_t}{\sigma_k} \frac{\partial \bar{u}'_i \bar{u}'_j}{\partial x_k} \right)}_{D_{r,j}=\text{Turbulent Diffusion}} \\ &- \underbrace{\left( \bar{u}'_i \bar{u}'_k \frac{\partial \bar{u}_j}{\partial x_k} + \bar{u}'_j \bar{u}'_k \frac{\partial \bar{u}_i}{\partial x_k} \right)}_{P_{ij}=\text{Stress Production}} \\ &- \underbrace{C_1 \frac{\varepsilon}{k} \left[ \bar{u}'_i \bar{u}'_j - \frac{2}{3} \delta_{ij} k \right] - C_2 \left[ P_{ij} - \frac{2}{3} \delta_{ij} P \right]}_{\phi_{ij}=\text{Pressure Strain}} - \underbrace{\frac{2}{3} \delta_{ij} \varepsilon}_{\varepsilon_{ij}=\text{Dissipation}} \end{aligned} \quad (3)$$

where the empirical constants  $\sigma_k = 1.0$ ,  $C_1 = 1.8$  and  $C_2 = 0.6$  [23]. The transport equation of the turbulence dissipation rate,  $\varepsilon$ , is as follows,

$$\frac{\partial \varepsilon}{\partial t} + \bar{u}_j \frac{\partial \varepsilon}{\partial x_j} = \frac{\partial}{\partial x_j} \left[ \left( \nu + \frac{\nu_t}{\sigma_\varepsilon} \right) \frac{\partial \varepsilon}{\partial x_j} \right] - C_{\varepsilon 1} \frac{\varepsilon}{k} \bar{u}'_i \bar{u}'_j \frac{\partial \bar{u}_i}{\partial x_j} - C_{\varepsilon 2} \frac{\varepsilon^2}{k} \quad (4)$$

where the empirical constants  $\sigma_\varepsilon = 1.3$ ,  $C_{\varepsilon 1} = 1.44$  and  $C_{\varepsilon 2} = 1.92$ . In the near-wall region, the two-layer zonal model with enhanced wall function was adopted to calculate turbulent air flow fields to enable accurate simulation of particle deposition [24]. The Wolfstein's one-equation model [25] was employed in the viscosity-affected near-wall region. The turbulent viscosity is calculated by,

$$\mu_{t,2layer} = \rho C_\mu l_\mu \sqrt{k} \quad (5)$$

Moreover, the dissipation rate  $\varepsilon$  is computed as follows,

$$\varepsilon = \frac{k^{3/2}}{l_\varepsilon} \quad (6)$$

where the length scales  $l_\mu$  and  $l_\varepsilon$  in the Eqs. (5) and (6) are calculated referring to Chen and Patel [26]. The turbulent viscosity in Eq. (5) is blended with the high Reynolds number  $\mu_t$  defined in the outer region, as proposed by Jongen [27],

$$\mu_{t,enh} = \lambda_\varepsilon \mu_t + (1 - \lambda_\varepsilon) \mu_{t,2layer} \quad (7)$$

where  $\lambda_\varepsilon$  is the blending function.

For the particle phase, DPM is employed to track the motion of each particle. All particles are assumed to be spherical solids. The influences of particles on the flows and the particle–particle collisions are ignored because the particle flow in this study is sufficiently dilute. The governing equation of particle phase can be written as,

$$\begin{aligned} \frac{du_p}{dt} &= \frac{1}{\tau} \frac{C_D \text{Re}_p}{24} (u_g - u_p) + \frac{g(\rho_p - \rho_g)}{\rho_p} + \zeta \sqrt{\frac{\pi S_0}{\Delta t}} \\ &+ \frac{2\rho K_C \nu^{0.5}}{\rho_p d_p (S_{lk} S_{kl})} s_{ij} (u - u_p) \end{aligned} \quad (8)$$

where  $u_g$  and  $\rho_g$  are the fluid velocity and density, respectively.  $u_p$  and  $\rho_p$  are the particle velocity and density, respectively. The right-hand side of the equation is the drag force term, the gravity and buoyancy term, the Brownian force term and the Saffman's lift force term, respectively. The particle relaxation time is calculated as follows,

$$\tau = \frac{Sd_p^2 C}{18\nu} \quad (9)$$

where  $S$  is the ratio of particle-to-fluid density. The Cunningham slip correction factor  $C_C$  was calculated using [28],

$$C_C = 1 + \frac{2\lambda}{d_p} \left( 1.257 + 0.4e^{-(1.1d_p/2\lambda)} \right) \quad (10)$$

The drag coefficient  $C_D$  is given by,

$$C_D = \begin{cases} \frac{24}{Re_p}, & \text{for } Re_p < 1 \\ \frac{24}{Re_p} \left( 1 + 0.15Re_p^{0.687} \right), & \text{for } 1 < Re_p < 400 \end{cases} \quad (11)$$

## 2.2. Turbulent dispersion of particles

It has been found that the turbulent dispersion of particles is crucial for simulating particle deposition. In this study, particle turbulent dispersion was modeled by the Discrete Random Walk Model (DRW), which is characterized by a Gaussian distributed random velocity fluctuation of fluids and a time scale of turbulent eddy [24]. The instantaneous fluid velocity fluctuation was obtained using,

$$u' = \zeta u'_{rms}, \quad v' = \zeta v'_{rms}, \quad w' = \zeta w'_{rms} \quad (12)$$

where  $u'_{rms}$ ,  $v'_{rms}$  and  $w'_{rms}$  are velocity fluctuations and  $\zeta$  is a normally distributed random number.

It was found that significant over prediction of particle deposition rate occurs if directly applying the DRW model with RSM model [15,16]. However, an effective method to accurately predict particle deposition velocity is to correct the wall-normal turbulent fluctuation in the near-wall region by DNS data, as only the velocity fluctuation normal to the wall is important for calculation of particle deposition velocity [15–17]. For particle deposition in a smooth duct air flow, the correction of wall-normal velocity fluctuation  $v'_{rms}$  from the DNS data by Kim et al. [29] is given by equation (10):

$$\frac{v'_{rms}}{u^*} = C(y^+)^2, \quad \text{for } y^+ < 4 \quad (13)$$

where  $u^*$  is frictional velocity, and the value of the constant  $C$  is 0.008. The dimensionless distance from the wall  $y^+$  is defined by,

$$y^+ = \frac{yu^*}{\nu} \quad (14)$$

For particle deposition in a ribbed duct air flow, Eq. (12) was adopted. This equation has been successfully applied for multilayer deposition simulation of a ribbed duct flow by Lericain et al. [10], as follows:

$$\frac{v'_{rms}}{u^*} = \frac{a_1 y^+}{1 + b_1 y^+ + c_1 y^{+2.41}}, \quad \text{for } y^+ < 30 \quad (15)$$

where  $a_1 = 0.0116$ ,  $b_1 = 0.203$  and  $c_1 = 0.0014$ .

## 2.3. Particle deposition velocity calculation

Particle deposition rate is commonly evaluated through the non-dimensional deposition velocity versus dimensionless particle relaxation time [30,31]. The dimensionless particle deposition velocity can be calculated by,

$$V_d^+ = \frac{V_d}{u^*} \quad (16)$$

where the frictional velocity  $u^*$  is calculated as,

$$u^* = \sqrt{\tau_w / \rho_g} = U_{mean} \sqrt{f/2} \quad (17)$$

The particle deposition velocity is defined as follows,

$$V_d = \frac{J}{C_0} = \frac{N_d/t_d/A}{N_0/V} = \frac{N_d/t_{max}}{N_0/h} \quad (18)$$

where  $J$  is the number of deposited particles per unit time and unit area of the surface, and  $C_0$  is the mean particle concentration.

Particle relaxation time is a time scale characterizing the adjustment of particle velocity to a changing fluid velocity [15,16]. The dimensionless particle relaxation time can be calculated by,

$$\tau_p^+ = \frac{C_C S d_p^2 u^{*2}}{18 \nu^2} \quad (19)$$

## 3. Case description and solution methods

**Fig. 1** (a) and (b) show the two-dimensional computational ducts with smooth and ribbed walls, respectively. The ducts are 0.02 m high and 0.4 m long, which are consistent with the cases in the literature for further comparison [15,16]. For the ribbed duct cases, the first half of the duct was smooth to ensure full development of turbulent air flow, while repeated ribs were arranged in the second half of the duct walls with identical spacing in the streamwise direction. The rib spacing and height are two crucial parameters which significantly influence the particle deposition rate and the flow pressure drop. In this study, the ratios of rib spacing to rib height  $p/e$  were designed to be 2, 4, 6, 8 and 10. The ratios of rib height to duct diameter  $e/D$  were 0.05, 0.1 and 0.2. The detailed computational cases are shown in **Table 1**. The air dynamic viscosity  $\mu$  is  $1.789 \times 10^{-5}$  kg s/m and the air density is 1.225 kg/m<sup>3</sup> at  $T = 288$  K. The air flow velocity is 5.5 m/s. The ratio of particle density to fluid density  $S$  is 2000. In the calculation, 30,000 uniformly distributed spherical particles were released into the flow field at  $X = 0.2$  after turbulent air flow had been fully developed. Particle diameters of 1, 2, 3, 5, 10, 20, 30 and 50  $\mu\text{m}$  were studied, as shown in **Table 1**. The initial particle velocities were equal to the mean velocity of the air flow. The gravity force is parallel to the air flow direction.

Structured grids were developed to discretize the smooth and ribbed duct surfaces by the software ANSYS ICEM 13.0. To accurately solve the complex turbulent flow in the boundary layer, the grids are clustered near the ribs and walls. The first grids are 0.05 mm away from the wall and the ribs. The dimensionless distance from the wall  $y^+$  for the first grids is about 1.13. The growth factor of the grid spacing from the walls to the center region is 1.2 in wall-normal direction. The grid numbers for Case A to Case H are 32,000, 287,797, 191,170, 143,833, 119,674, 101,251, 106,717 and 72,010, respectively. The computational grids near the wall for the smooth duct (Case A), the ribbed duct with  $p/e = 2$  and  $e/D = 0.1$  (Case B) and the ribbed duct with  $p/e = 6$  and  $e/D = 0.1$  (Case D) are shown in **Fig. 2**.

In addition, fully developed velocity and T.K.E. profiles were imposed at the duct inlet for both smooth and ribbed duct cases by user-defined-function (UDF) codes. The one seventh power law [15,16] was adopted by,

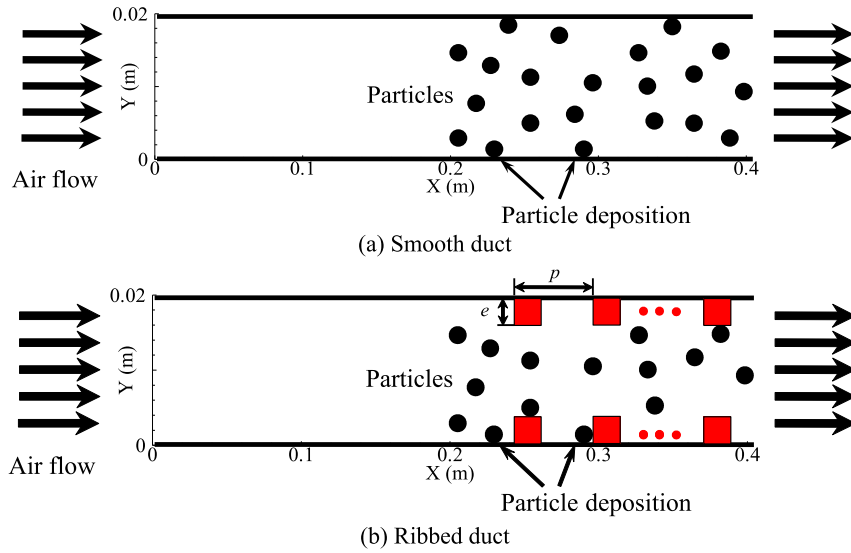


**Fig. 1.** Schematic of particle deposition in smooth and ribbed ducts.

$$U = U_{free} \left( \frac{y}{D/2} \right)^{1/7} \text{ for } y \leq D/2 \quad (20)$$

$$U = U_{free} \left( \frac{h-y}{D/2} \right)^{1/7} \text{ for } y > D/2 \quad (21)$$

$$U_{free} = \frac{8}{7} U_{mean} \quad (22)$$

where  $U_{mean}$  is the mean velocity of the duct air flow and  $D$  is the duct height. The T.K.E. value,  $k$  [15,16] is expressed as follows,

$$k = \frac{\tau_w}{\rho_g \sqrt{C_\mu}} + \frac{y}{D/2} \left( 0.002 U_{free}^2 - \frac{\tau_w}{\rho_g \sqrt{C_\mu}} \right) \text{ for } 0 \leq y \leq D/2 \quad (23)$$

$$k = \frac{\tau_w}{\rho_g \sqrt{C_\mu}} + \frac{D-y}{D/2} \left( 0.002 U_{free}^2 - \frac{\tau_w}{\rho_g \sqrt{C_\mu}} \right) \text{ for } D/2 < y \leq D \quad (24)$$

$$\tau_w = \frac{\rho_g U_{mean}^2}{2} \cdot f \quad (25)$$

where  $f$  is the fanning friction factor and is computed by,

$$f = 0.0791 \cdot Re^{-0.25} \quad (26) \quad (2,800 < Re < 105^2)$$

and Reynolds number  $Re$  is defined as,

$$Re = \frac{U_{free} D}{\nu} \quad (27)$$

In the realistic deposition process, a particle may either rebound from or remain attached to the surface when it impacts a surface [19]. Moreover, the attached particle may be re-suspended again in the air flow fields. Nevertheless, in this study, the particle rebound and re-suspension are not considered. It is assumed that all the particles will be attached to the surface and never be re-suspended once they impact the walls and the ribs. Moreover, this study investigates dry particle deposition in the adiabatic condition. Therefore, the effects of temperature and humidity on particle deposition are not considered here.

The finite volume method (FVM) was employed to solve the governing equations of turbulent air flow. The convection term was discretized using the second-order upwind scheme and the diffusion terms were discretized using the second-order central difference scheme. The Semi-Implicit Method for Pressure Linked Equations (SIMPLE) algorithm [32] was adopted to deal with the pressure and velocity coupling. The particle equations of motion were solved by the Runge-Kutta method. The turbulent velocity fluctuation corrections as well as the boundary conditions in the duct inlet for smooth and ribbed wall cases were imposed into FLUENT using UDF codes.

**Table 1**  
Computational cases.

Case no.	Air velocity (m/s)	Particle diameter ( $\mu\text{m}$ )	Surface type	Rib height ( $e/D$ )	Rib spacing ( $p/e$ )
A (1–8)	5.5	1,2,3,5,10,20,30,50	Smooth	/	/
B (9–16)	5.5	1,2,3,5,10,20,30,50	Ribbed	0.1	2
C (17–24)	5.5	1,2,3,5,10,20,30,50	Ribbed	0.1	4
D (25–32)	5.5	1,2,3,5,10,20,30,50	Ribbed	0.1	6
E (33–40)	5.5	1,2,3,5,10,20,30,50	Ribbed	0.1	8
F (41–48)	5.5	1,2,3,5,10,20,30,50	Ribbed	0.1	10
G (49–56)	5.5	1,2,3,5,10,20,30,50	Ribbed	0.05	10
H (57–64)	5.5	1,2,3,5,10,20,30,50	Ribbed	0.2	10

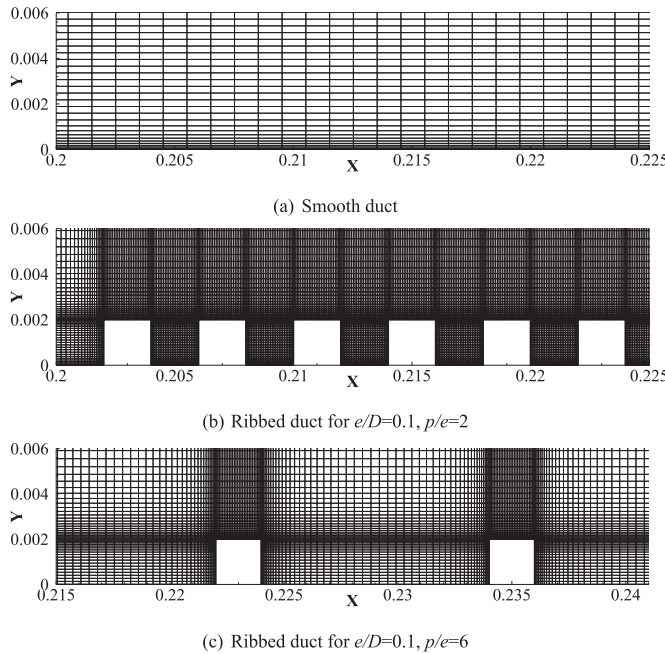


Fig. 2. Structural grids for smooth and ribbed ducts near the wall.

## 4. Results and discussion

### 4.1. Air-particle flow simulations and numerical validation

Firstly, the turbulent air flow fields for smooth duct were verified according to the DNS results. Fig. 3 compares the present mean and fluctuating air velocities with DNS data by Kim et al. [29]. The mean and fluctuating velocities were obtained at  $X = 0.3$  m as the flow had reached fully developed state at that position. From Fig. 3 (a), it can be seen that the calculated mean air velocity agrees well with the DNS results. Furthermore, the present fluctuating velocities in both streamwise and wall-normal directions are also in good agreement with the literature data, as shown in Fig. 3 (b). The above agreements imply that the solution of air flow fields for smooth-wall duct is correct and creditable.

Moreover, the air flow fields for the ribbed ducts were also verified against experimental results in the literature [33]. The ratio of rib spacing to rib height  $p/e$  is 10 and the ratio of rib height to duct diameter  $e/D$  is 0.1. The air velocity profiles from ten streamwise positions between the 8th and 9th ribs were obtained and compared with measured data, as shown in Fig. 4. It can be observed that the present calculated velocity profiles are highly consistent with the literature results, which indicates that the present RSM with turbulent fluctuation correction can simulate the turbulent flow in ribbed-surface duct very well. Furthermore, the air flow velocity fields in smooth and ribbed ducts were obtained and are given in Fig. 5. Clear turbulent boundary layers can be observed for smooth and ribbed duct flows. In addition, there were 98, 48, 32, 24, 18, 38 and 8 surface ribs on the walls for Case B to Case H, respectively. The recirculation zones in the cavity between two adjacent surface ribs were also correctly simulated, as shown in Fig. 5 (b). Therefore, the above validations prove that the turbulent air flow fields are accurately resolved by the present CFD models both for smooth and ribbed ducts.

Further, the particle deposition velocities for smooth duct cases were compared with the experimental results by Friedlander & Johnstone [34], Liu & Agarwal [35] and El-Shobokshy [36], as shown in Fig. 6. The dimensionless deposition velocity was

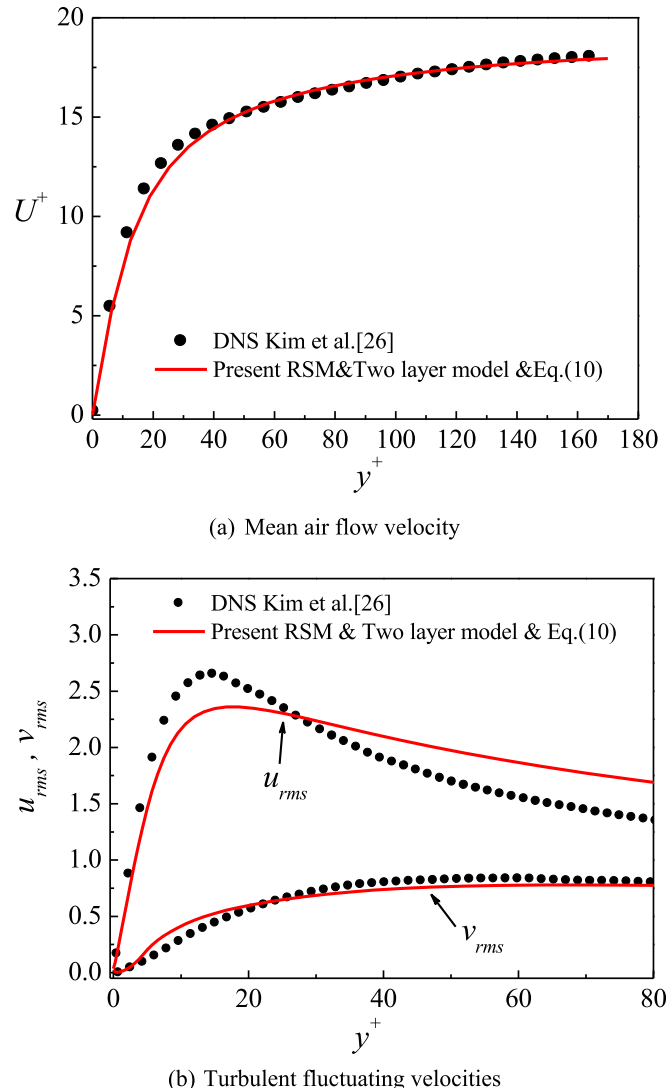


Fig. 3. Comparison of flow velocity profiles for smooth duct with DNS data.

normalized by frictional velocity of air flow and the dimensionless particle relaxation time was calculated by Eq. (16). It can be found that dimensionless particle relaxation time  $\tau_p^+$  is directly proportional with the square of the particle diameter  $d_p^2$ . Therefore, the dimensionless particle relaxation time is increased with the increase of particle diameter. The dimensionless particle deposition velocity first increases significantly, and then keeps constant with the increase of dimensionless particle relaxation time. This is because the influence of turbulent eddy motions on particle deposition is weakened and the particle inertia becomes crucial for

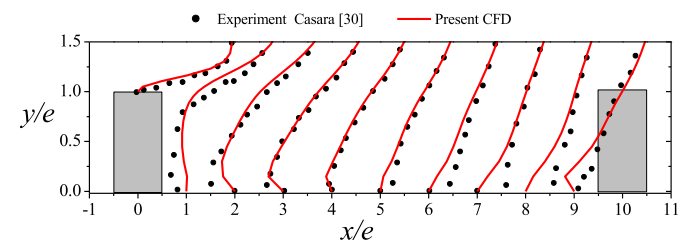
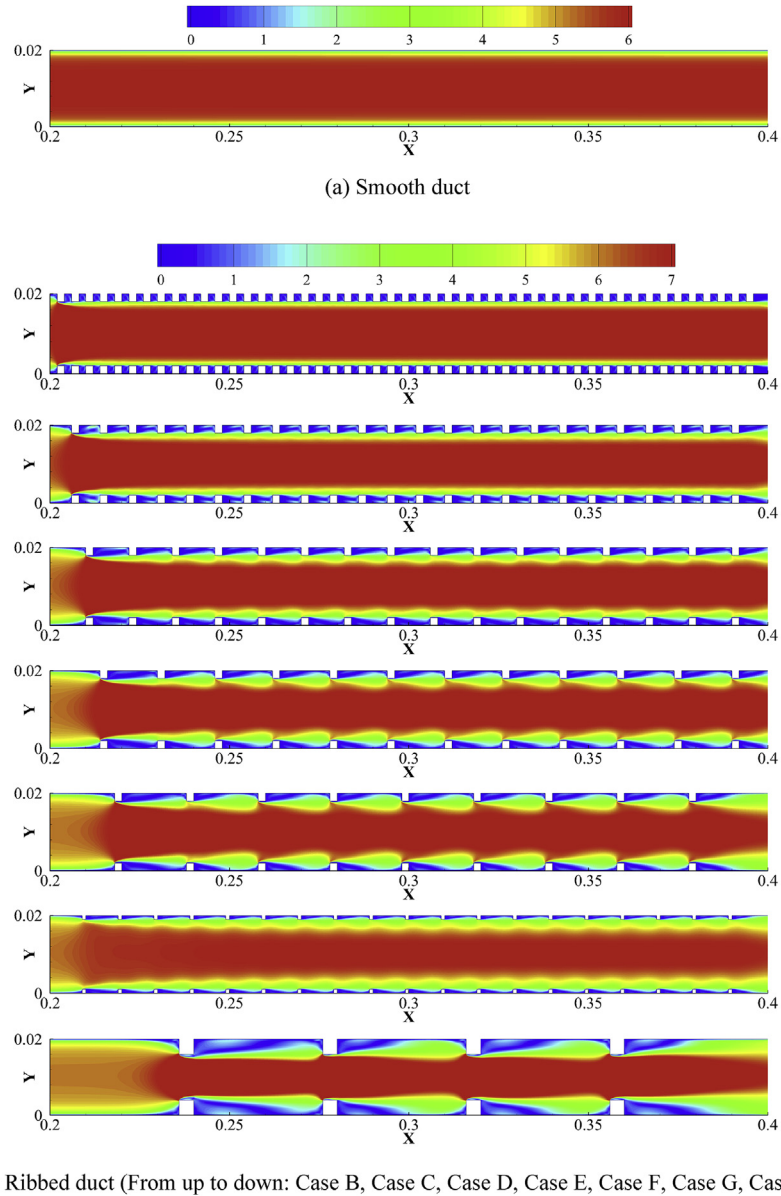


Fig. 4. Comparison of flow velocity profiles for ribbed duct with experimental data.



(b) Ribbed duct (From up to down: Case B, Case C, Case D, Case E, Case F, Case G, Case H)

**Fig. 5.** Velocity fields of air flow in smooth- and ribbed ducts.

large particles. It can be seen that the particle deposition velocity profile obtained by the present simulation is in very good agreement with the literature data. As a consequence, the present numerical methods can predict particle deposition process accurately.

#### 4.2. Effects of rib spacing and height on particle deposition

To investigate the effects of rib spacing and height on particle deposition velocity, Fig. 7 (a) and (b) show the particle deposition velocities in ribbed duct flows with different rib spacings and heights, respectively. The results were also compared with the smooth duct case. It can be observed that the particle deposition velocity is significantly increased by surface ribs by several orders of magnitude. Moreover, the enhancement of particle deposition velocity differs significantly for different particle relaxation times. Generally, the deposition enhancement for small particles ( $\tau_p^+ < 1$ ) is much higher than that for large particles ( $\tau_p^+ > 1$ ). When  $\tau_p^+ < 1$ , the dimensionless particle deposition velocity can be increased by almost four orders of magnitude for the ribbed surface, while it is

only enhanced by about two orders of magnitude when  $\tau_p^+ > 1$ . This is because small particles are much more easily captured by the turbulent eddies and entrained by the wall. The detailed mechanism of particle deposition enhancement for different rib spacings and heights is discussed in the Section 5.

To observe the particle deposition enhancement more clearly, an enhancement ratio  $\gamma$  was defined as Eq. (28) and the results are given in Fig. 8.

$$\gamma = \frac{v_d \text{ rough}}{v_{dsmooth}} \quad (28)$$

The  $\gamma$  is the ratio of the dimensional particle deposition velocities between ribbed and smooth duct cases, which represents the pure enhancement of particle deposition by surface ribs without considering the increase of flow drag. The comprehensive efficiency of particle deposition by the ribbed wall was investigated and discussed in the section below.

For different rib spacings, it can be observed that the particle deposition enhancement is quite similar when  $\tau_p^+ < 1$ , while

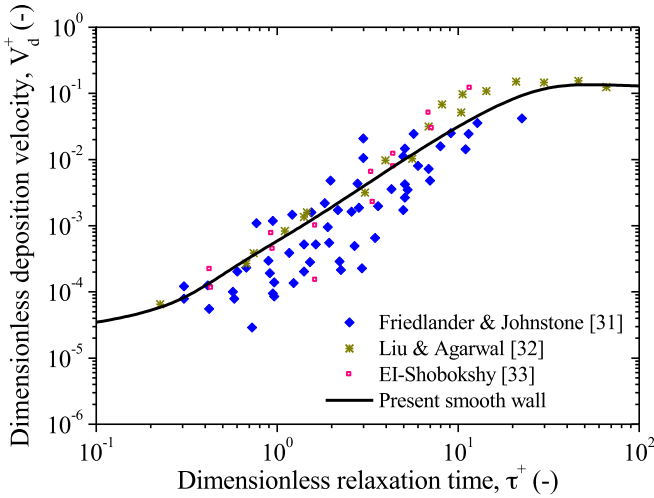
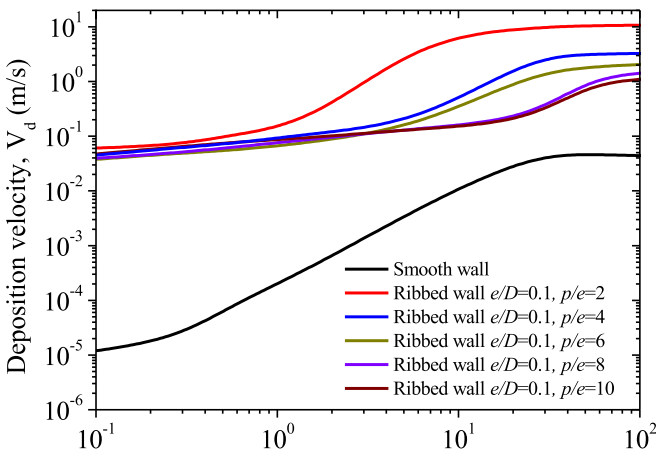


**Fig. 6.** Validation of particle deposition velocity in air duct flow with smooth wall.

obvious differences appear when  $\tau_p^+ > 1$ . The maximum



(a) Different rib spacings

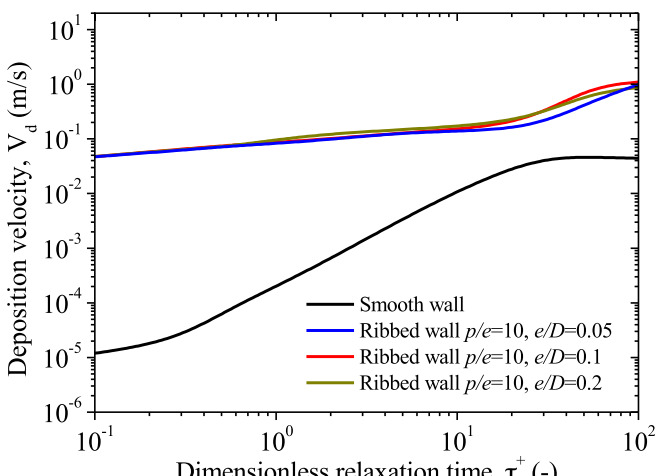
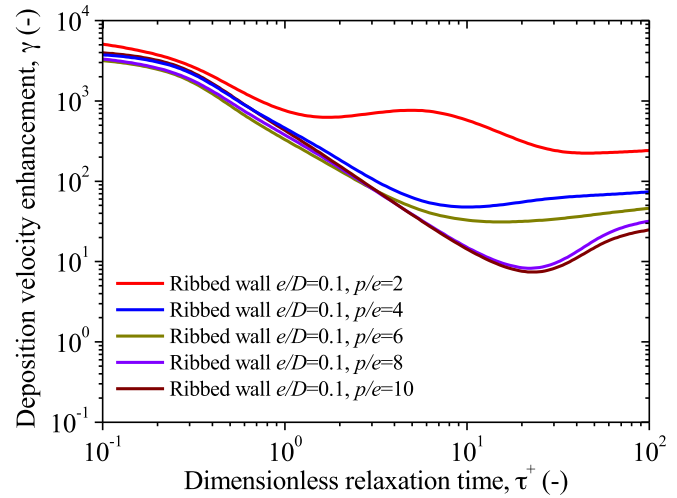
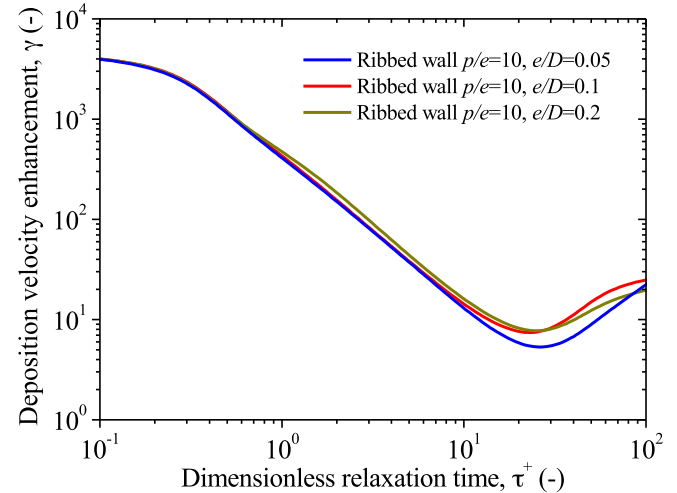


**Fig. 7.** Particle deposition velocity in ribbed duct flow with different rib spacings and heights.



(a) For different rib spacings



(a) For different rib heights

**Fig. 8.** Particle deposition enhancement by ribbed surface with different rib spacings and heights.

enhancement ratio is obtained for rib spacing  $p/e = 2$  (Case B), as shown in Fig. 8 (a). This is because more ribs are arranged on the walls for small rib spacing. Therefore, more particles are intercepted by the windward surfaces of the ribs and the particle deposition area is also significantly increased. The maximum enhancement ratio of particle deposition can reach about 5700 times for particle diameters with  $1 \mu\text{m}$  and about 250 times for particle diameters with  $30 \mu\text{m}$ . For different rib heights, no significant distinction can be seen on particle deposition enhancement ratio, as shown in Fig. 8 (b). Although more particles are intercepted by the higher surface ribs, many more ribs are arranged on the wall when rib heights are small. Therefore, the increase of deposition area is more or less the same regardless of rib height. Consequently, particle deposition enhancement is increased with the decrease of rib spacing while rib height has no obvious influence on particle deposition enhancement.

#### 4.3. Efficiency ratio of particle deposition enhancement

Although surface ribs can significantly enhance particle deposition as discussed above, more flow drag is induced by the ribs. To

consider both effects simultaneously, an efficiency ratio of particle deposition enhancement by surface ribs  $\eta$  is defined as follows,

$$\eta = \frac{v_d \text{ rough}}{v_{d\text{smooth}}} \cdot \frac{f_{\text{smooth}}}{f_{\text{rough}}} \quad (29)$$

where the parameter  $f_{\text{rough}}/f_{\text{smooth}}$  represents increase of flow drag.

**Fig. 9** shows the increase of flow drag  $f_{\text{rough}}/f_{\text{smooth}}$  for different rib spacings and heights. From **Fig. 9** (a), it can be seen that the increase of flow drag reaches its peak value when the rib spacing is 6 and 8. This result is consistent with the experimental measurements of Zhang et al. [37]. The maximum drag for ribbed duct flow is about 11 times that for smooth duct flow. Moreover, the flow drag dramatically increases with the increase of rib height, as is to be expected.

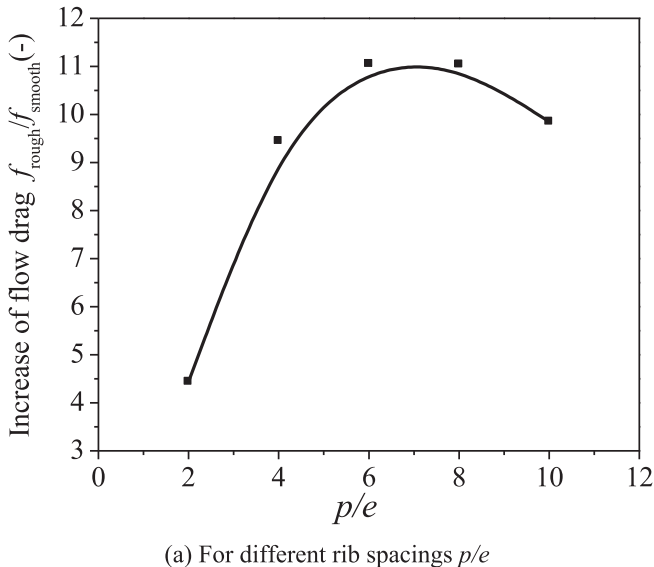
**Fig. 10** (a) and (b) illustrate the efficiency ratio of particle deposition enhancement for different rib spacings and heights, respectively. From **Fig. 10** (a), it can be observed that the efficiency ratio for  $p/e = 2$  is much higher than for other rib spacings. This is because the particle deposition enhancement ratio is high while

the increase of flow drag is small at this rib spacing. Furthermore, as the particle deposition enhancement ratio is about the same for different rib heights while the flow drag is much lower for smaller rib heights, the efficiency ratio is higher for smaller rib heights as shown in the **Fig. 10** (b). In this study, the maximum efficiency ratio of particle deposition enhancement can reach 1000 for small particles ( $\tau_p^+ < 1$ ) while it can also be 100 for large particles ( $\tau_p^+ > 1$ ) when rib spacing is  $p/e = 2$  and rib height  $e/D = 0.1$ . Therefore, surface ribs are an efficient and effective alternative for particle deposition enhancement, especially for small particles ( $\tau_p^+ < 1$ ).

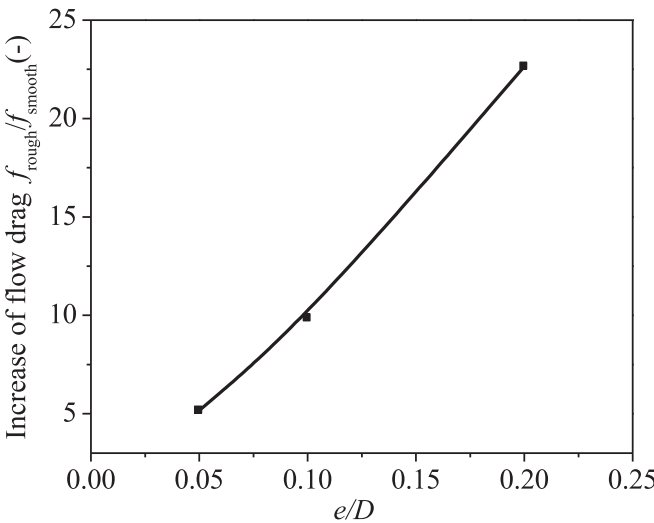
## 5. Mechanisms of deposition enhancement by surface ribs

In this section, investigations of the mechanisms of particle deposition enhancement by surface ribs with different spacings and heights are described and discussed. According to the author's previous study [5], the three main particle deposition enhancement mechanisms are: 1. the interception by the windward rib surfaces, 2. the increase of deposition area and 3. the entrainment of turbulent eddies induced by the surface ribs.

The interception by the windward surface of the ribs is the most important mechanism for particle deposition enhancement by ribs.

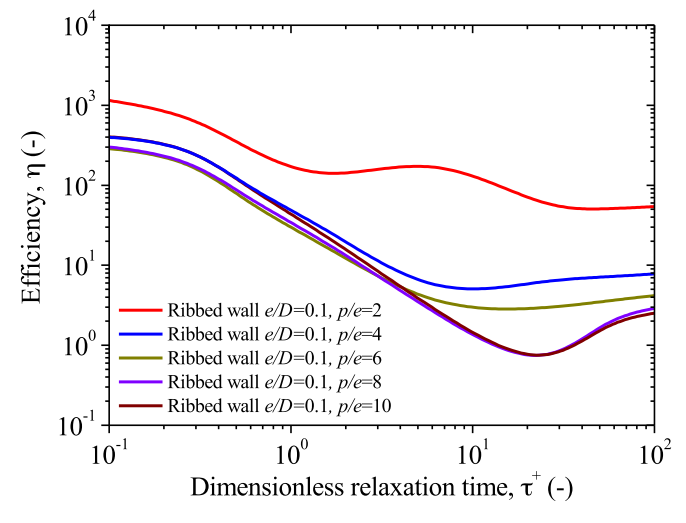


(a) For different rib spacings  $p/e$

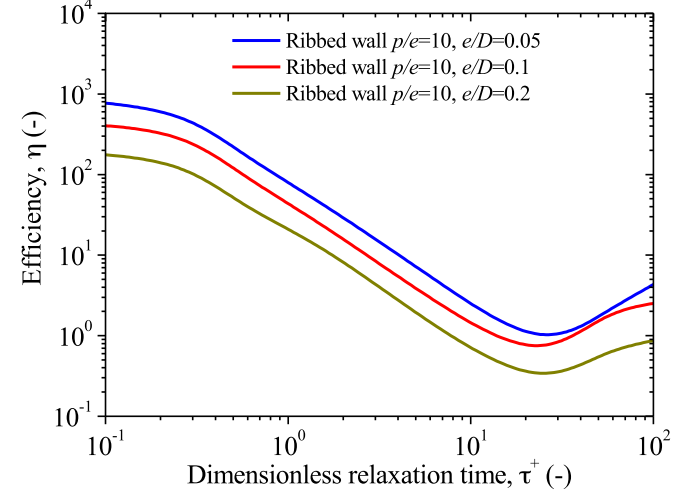


(b) For different rib heights  $e/D$

**Fig. 9.** Increase of flow drag by ribbed surface with different spacings and heights.



(a) For different rib spacings



(b) For different rib heights  $e/D$

**Fig. 10.** Efficiency ratio of particle deposition by ribbed wall.

The number of particles obstructed is directly proportional to the windward surface area. For Cases A to H the two-dimensional windward surface area of the ribs are 0.196, 0.096, 0.064, 0.048, 0.036, 0.038 and 0.032 m, respectively. Therefore, the windward surface area is significantly influenced by rib spacing but almost unaffected by rib height. The maximum windward surface area occurs when  $p/e = 2$  and  $e/D = 0.1$  (Case B).

At the same time, the total deposition area is also increased by both the windward and leeward surfaces of the ribs. The two-dimensional increase of deposition area for different rib spacings and heights is 0.392, 0.192, 0.128, 0.096, 0.072, 0.076 and 0.064 m for ribbed surface Cases B to G, respectively. The basic deposition area of the smooth duct case is 0.4 m. Therefore, the increased ratios of deposition area are 98%, 48%, 32%, 24%, 18%, 19% and 16% for ribbed duct Cases B to H, respectively. The maximum increase of deposition area is generated for  $p/e = 2$  and  $e/D = 0.1$  (Case B), which is similar to the result for the windward rib surface areas.

The other important mechanism for particle deposition enhancement is the capture and entrainment by turbulent eddies to the wall. To describe this mechanism clearly, Fig. 11 shows turbulent kinetic energy (T.K.E.) distribution overlaying the air flow streamlines both for smooth and ribbed duct cases. It can be seen that the turbulent structures for ribbed ducts are quite different to those for the smooth duct. In the latter case, the flow is along the streamwise direction and the T.K.E. value near the wall is very small. These are not favorable conditions for particle deposition. For ribbed ducts, there is one eddy in the cavity between two nearby surface ribs when the rib spacing  $p/e$  is 2. The cavity is filled by the eddy and the momentum exchange between the cavity eddy and the outer flow is very weak, as shown in Fig. 11 (b). The T.K.E. near the surface ribs is higher than that for smooth duct flow but is still small. When the rib spacing  $p/e$  increases to 4, it can be seen that the cavity is filled by a small eddy, together with a large eddy. The momentum exchange between the cavity flow and the outer flow is

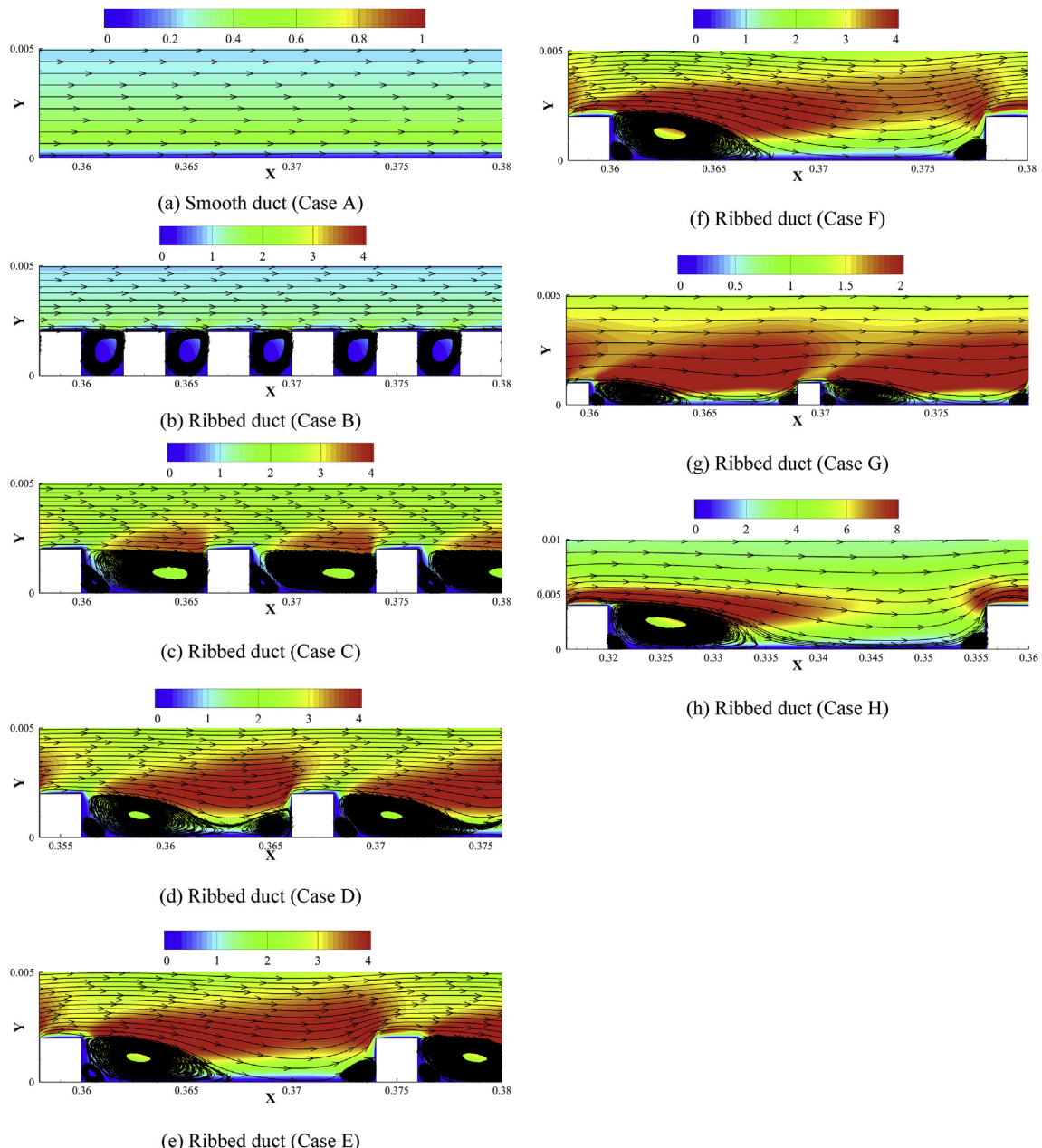


Fig. 11. T.K.E. distribution and streamlines of air flow in smooth and ribbed ducts.

also weak. However, there are large T.K.E. areas above the cavity (the red color (in web version) in the figure). This is valuable for particle turbulent dispersion and deposition. When the rib spacing  $p/e$  is 6, the essential difference can be observed and shows that the flow separation and attachment take place within the cavity between two adjacent ribs. There are a large separation eddy and a small attachment eddy in the cavity causing strong momentum exchange to occur between the cavity flow and the outer flow. It is noted that the T.K.E. above the cavity is much larger. When the rib spacing  $p/e$  are 8 and 10, separation and attachment eddies exist, as well as strong momentum exchange as the distance between them becomes greater. The largest T.K.E. distribution occurs for the rib spacing  $p/e = 10$ . Obviously, the strong momentum exchange and large T.K.E. value near the wall are beneficial for particle deposition enhancement as many particles would be captured by the turbulent eddies and entrained to the wall for deposition. For different rib heights, it can be seen that the turbulent structures are not significantly changed, as shown in Fig. 11 (f), (g) and (h). However, much larger T.K.E. distribution are generated by the higher surface ribs. For small particles ( $\tau_p^+ < 1$ ), the interception by the windward surface of the ribs is intense while the entrainment of turbulent eddies is weak when the rib spacing is small. The situation is just the opposite when the rib spacing is large. Therefore, the particle deposition enhancement ratios are not obviously different for different rib spacings under the combined effects when  $\tau_p^+ < 1$ . However, the capture and entrainment effects by turbulent eddies become very weak for large particles because of their larger inertias. The main deposition enhancement mechanism for large particles is the interception of surface ribs. Therefore, the particle deposition enhancement ratio is much higher for ducts with close rib spacing when  $\tau_p^+ > 1$ . The effects of the above two mechanisms are more or less the same for different rib heights. Hence no obvious differences are observed in particle deposition enhancement when the rib height changes.

## 6. Conclusions and future work

In the study, the effects of surface rib spacings and heights on particle deposition enhancement were numerically investigated based on the RSM and DPM models combined with UDF corrections. The mechanisms of particle deposition enhancement and deposition efficiency ratios were analyzed and discussed for different particle sizes, rib spacings and rib heights. The following conclusions can be drawn.

1. Particle deposition velocity is significantly enhanced by the presence of surface ribs by factors ranging between about 250 and 5700. The deposition enhancement ratio is more efficient for small particles ( $\tau_p^+ < 1$ ). This is because the capture and entrainment of turbulent eddies induced by surface ribs are more effective for small particles, except for the interception effects of surface ribs.
2. Particle deposition enhancement increases as rib spacing decreases, especially for large particles ( $\tau_p^+ > 1$ ), but there is no obvious effect due to rib heights. The deposition enhancement ratio is the highest when rib spacing  $p/e = 2$ .
3. The interception by the windward surface of ribs, increases of deposition area and the entrainment of turbulent eddies to the wall are the three main mechanisms for particle deposition enhancement by surface ribs. The first two mechanisms are effective for small rib spacing while the third mechanism is strongest for large rib spacing. No significant difference can be found between the three mechanisms for different rib heights.
4. When the particle deposition enhancement and increase of flow drag is considered together, the efficiency ratio is higher for

smaller rib spacing and lower rib height due to the smaller form drag. The maximum efficiency ratio can reach about 1000 for small particles ( $\tau_p^+ < 1$ ) and about 100 for large particles ( $\tau_p^+ > 1$ ) when  $p/e = 2$  and  $e/D = 0.1$ . Therefore, a ribbed surface is efficient for particle deposition enhancement.

Particle deposition in three-dimensional ribbed ducts needs to be investigated, which is closer to practical engineering applications. In addition, re-suspension effects should also be considered in future work, as this may weaken particle deposition rates [38–40].

## Acknowledgment

The authors appreciate the financial supports provided by the Central Policy Unit of the Hong Kong Government via the Public Policy Research Scheme (2013.A6.010.13A).

## References

- [1] Vincent JH, MacLennan ASM. Aerodynamic considerations in electrostatic precipitator. *J Electrost* 1980;8:325–42.
- [2] Suh YJ, Kim SS. Effect of obstructions on the particle collection efficiency in a two-stage electrostatic precipitator. *J Aerosol Sci* 1996;27:61–74.
- [3] Lai ACK, Byrne MA, Goddard AJH. Measured deposition of aerosol particles on a two-dimensional ribbed surface in a turbulent duct flow. *J Aerosol Sci* 1999;30:1201–14.
- [4] Lai ACK, Byrne MA, Goddard AJH. Enhanced particle loss in ventilation duct with ribbed surface. *Build Environ* 2000;35:425–32.
- [5] Lu H, Lu L. Numerical investigation on particle deposition enhancement in duct air flow by ribbed wall. *Build Environ* 2015;85:61–72.
- [6] Barth T, Reiche M, Banowski M, Oppermann M, Hampel U. Experimental investigation of multilayer particle deposition and resuspension between periodic steps in turbulent flows. *J Aerosol Sci* 2013;64:111–24.
- [7] Li A, Ahmadi G. Computer simulation of deposition of aerosols in a turbulent channel flow with rough walls. *Aerosol Sci Technol* 1993;18:11–24.
- [8] Li A, Ahmadi G, Bayer RG, Gaynes MA. Aerosol particle deposition in an obstructed turbulent duct flow. *J Aerosol Sci* 1994;25:91–112.
- [9] Iacono GI, Tucker P, Reynolds A. Predictions for particle deposition from LES of ribbed channel flow. *Int J Heat Fluid Flow* 2005;26:558–68.
- [10] Lericain G, Drapeau-Martin S, Barth T, Hampel U. Numerical simulation of multilayer deposition in an obstructed channel flow. *Adv Powder Technol* 2014;25:310–20.
- [11] Chen Q. Ventilation performance prediction for buildings: a method overview and recent applications. *Build Environ* 2009;44(4):848–58.
- [12] Sun K, Lu L. Particle flow behavior of distribution and deposition throughout 90° bends: analysis of influencing factors. *J Aerosol Sci* 2013;65:26–41.
- [13] Sun K, Lu L, Jiang H, Jin HH. Experimental study of solid particle deposition in 90° ventilated bends of rectangular cross section with turbulent flow. *Aerosol Sci Technol* 2013;47:115–24.
- [14] Zhang Z, Chen Q. Comparison of the Eulerian and Lagrangian methods for predicting particle transport in enclosed spaces. *Atmos Environ* 2007;41:5236–48.
- [15] Zhang Z, Chen Q. Prediction of particle deposition onto indoor surfaces by CFD with a modified Lagrangian method. *Atmos Environ* 2009;43:319–28.
- [16] Tian L, Ahmadi G. Particle deposition in turbulent duct flows—comparisons of different model predictions. *J Aerosol Sci* 2007;38:377–97.
- [17] Gao NP, Niu JL. Modeling particle dispersion and deposition in indoor environments. *Atmos Environ* 2007;41:3862–76.
- [18] Gao N, Niu J, He Q, Zhu T, Wu J. Using RANS turbulence models and Lagrangian approach to predict particle deposition in turbulent channel flows. *Build Environ* 2012;48:206–14.
- [19] Jiang H, Lu L, Sun K. Simulation of particle deposition in ventilation duct with a particle-wall impact model. *Build Environ* 2010;45(5):1184–91.
- [20] Jiang H, Lu L, Sun K. Experimental study and numerical investigation of particle penetration and deposition in 90 degrees bent ventilation ducts. *Build Environ* 2011;46:2195–202.
- [21] Sun K, Lu L, Jiang H. A computational investigation of particle distribution and deposition in a 90° bend incorporating a particle-wall model. *Build Environ* 2011;46:1251–62.
- [22] Sun K, Lu L, Jiang H. A numerical study of bend-induced particle deposition in and behind duct bends. *Build Environ* 2012;52:77–87.
- [23] Launder BE, Reece GJ, Rodi W. Progress in the development of a Reynolds stress turbulent closure. *J Fluid Mech* 1975;68(3):537–66.
- [24] FLUENT Inc. FLUENT 12.0 user's guide. 2009. Lebanon, NH.
- [25] Wolfstein M. The velocity and temperature distribution of one-dimensional flow with turbulence augmentation and pressure gradient. *Int J Heat Mass Transf* 1969;12(3):301–18.

- [26] Chen HC, Patel VC. Near-wall turbulence models for complex flows including separation. *AIAA J* 1988;26:641–8.
- [27] Jongen T. Simulation and modeling of turbulent incompressible flows. PhD thesis, Lausanne, Switzerland: EPF Lausanne; 1992.
- [28] Ounis H, Ahmadi G. Analysis of dispersion of small spherical particles in a random velocity field. *J Fluids Eng* 1990;112:114–20.
- [29] Kim J, Moin P, Moser R. Turbulence statistics in fully developed channel flow at low Reynolds number. *J Fluid Mech* 1987;177:133–66.
- [30] Guha AA. Unified Eulerian theory of turbulent deposition to smooth and rough surface. *J Aerosol Sci* 1997;28:1517–37.
- [31] Guha A. Transport and deposition of particles in turbulent and laminar flow. *Annu Rev Fluid Mech* 2008;40:311–41.
- [32] Partankar SV. Numerical heat transfer and fluid flow. Washington, DC: Hemisphere; 1980.
- [33] Casarsa L. Aerodynamic performance investigation of a fixed rib-roughened internal cooling passage. Ph.D. thesis. Belgium: Von Karman Institute for Fluid Dynamics; 2003.
- [34] Friedlander SK, Johnstone HF. Deposition of suspended particles from turbulent gas streams. *Ind Eng Chem* 1957;49:1151–6.
- [35] Liu BYH, Agarwal JK. Experimental observation of aerosol deposition in turbulent flow. *J Aerosol Sci* 1974;5:145–55.
- [36] El-Shobokshy MS. Experimental measurements of aerosol deposition to smooth and rough surfaces. *Atmos Environ* 1983;17:639–44.
- [37] Zhang HQ, Lu H, Wang B, Wang XL. Experimental investigation of flow drag and turbulence intensity of a channel flow with rough walls. *Chin Phys Lett* 2011;28(8):084703.
- [38] Zhao B, Wu J. Modeling particle deposition from fully developed turbulent flow in ventilation duct. *Atmos Environ* 2006;40:457–566.
- [39] Zhao B, Wu J. Modeling particle deposition onto rough walls in ventilation duct. *Atmos Environ* 2006;40:6918–27.
- [40] Zhou B, Zhao B, Tan ZC. How particle resuspension from inner surfaces of ventilation ducts affects indoor air quality—a modeling analysis. *Aerosol Sci Technol* 2011;45:996–1009.

## Nomenclature

$C_0$ : mean particle concentration

$D$ : duct height

$F_S$ : Saffman's lift force

$f$ : fanning friction factor  
 $f_{rough}$ : flow drag for rough duct  
 $f_{smooth}$ : flow drag for smooth duct  
 $J$ : number of particles deposited per unit time and unit area  
 $k$ : turbulent kinetic energy (T.K.E.)  
 $e$ : rib height  
 $\bar{p}$ : time-averaged pressure  
 $p$ : rib spacing  
 $Re$ : Reynolds number  
 $S$ : ratio of particle-to-fluid density  
 $T_L$ : fluid Lagrangian integral time scale  
 $U_{mean}$ : mean velocity of air  
 $U_{free}$ : freestream velocity of air  
 $u_g$ : velocity of fluid  
 $\bar{u}_i$ : time-averaged velocity  
 $u_p$ : velocity of particle  
 $u'_{rms}$ : streamwise fluctuating velocity of air  
 $V_d$ : particle deposition velocity  
 $V_d^+$ : dimensionless particle deposition velocity  
 $v_{d rough}$ : particle deposition velocity on ribbed duct  
 $v_{d smooth}$ : particle deposition velocity on smooth duct  
 $v'_{rms}$ : wall-normal fluctuating velocity of air  
 $w'_{rms}$ : spanwise fluctuating velocity of air  
 $u'$ : frictional velocity of air  
 $y^+$ : dimensionless distance from the wall

## Greek symbols

$\epsilon$ : dissipation rate of turbulent kinetic energy  
 $\rho_f$ : density of fluid  
 $\rho_p$ : density of particle  
 $\zeta$ : normal distributed random number  
 $\mu$ : dynamic viscosity of air  
 $\nu$ : kinematic viscosity of air  
 $\gamma$ : ratio of dimensional particle deposition velocities between ribbed and smooth duct cases  
 $\eta$ : a pressure drop-weighted particle deposition enhancement  
 $\tau_p^+$ : dimensionless particle relaxation time